ACS APPLIED ELECTRONIC MATERIALS

pubs.acs.org/acsaelm Article

Decoding Vibrational Contributions and Exciton Dynamics in TADF Emitters for Enhanced OLED Efficiency

Sanyam and Anirban Mondal*

Cite This: https://doi.org/10.1021/acsaelm.5c00286 Read Online

ACCESS | Metrics & More | Article Recommendations | Supporting Information

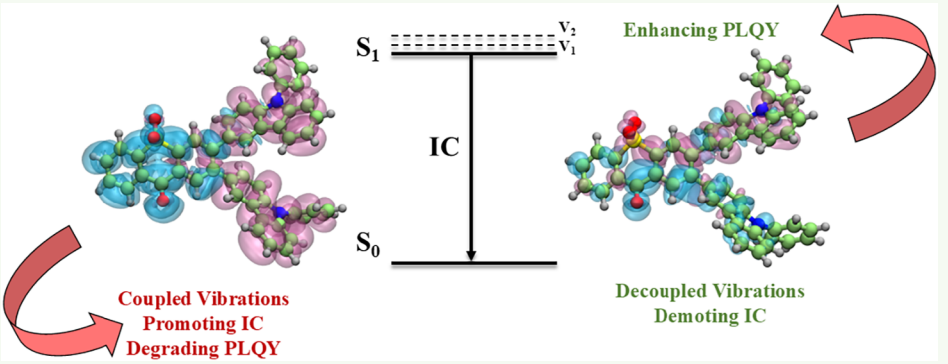

ABSTRACT: Thermally activated delayed fluorescence (TADF) compounds play a pivotal role in enhancing the efficiency of organic light-emitting diodes (OLEDs) by enabling effective triplet exciton utilization, often facilitated by vibrational assistance. While multiresonant TADF systems benefit from rigid planar structures that suppress nonradiative decay, traditional donor−acceptor−donor (D−A−D) systems are more prone to nonradiative losses with their flexible single-bond connections. This study investigates three structurally similar D−A−D TADF compounds with distinct external quantum efficiencies to uncover the factors influencing their performance. Our analysis identifies specific vibrational modes that either enhance radiative transitions or contribute to nonradiative decay, emphasizing the critical role of vibrational dynamics. Using Huang−Rhys factor and exciton−phonon coupling, we demonstrate how these vibrational modes govern exciton dynamics. The Herzberg−Teller effect emerges as a key mechanism driving thermally activated performance, with vibrational corrections significantly improving the accuracy of rate predictions. The computed radiative and nonradiative rates show satisfactory agreement with experimental data, validating the robustness of our computational protocol. These findings provide actionable insights into the molecular design of TADF emitters, offering strategies to optimize OLED performance by balancing the interplay between vibrational dynamics and electronic transitions.

KEYWORDS: *thermally activated delayed fluorescence, exciton, Huang−Rhys factor, exciton−phonon coupling, Herzberg−Teller effect*

1. INTRODUCTION

Thermally activated delayed fluorescence (TADF) emitters have garnered significant attention in organic light-emitting diodes (OLEDs) due to their ability to utilize triplet excitons efficiently.[1−3] Traditional emitters, such as fluorescent and phosphorescent materials, exhibit inherent limitations. Fluorescent materials achieve an internal quantum efficiency (IQE) of only 25%, while phosphorescent materials, though capable of harvesting triplet excitons, face challenges such as shorter device lifetimes due to prolonged exciton residence in the triplet (T_1) state. Additionally, phosphorescent materials often rely on heavy metal atoms (e.g., Ir, Pt, or Au), significantly increasing production costs. TADF materials address these limitations by enabling efficient triplet exciton utilization without heavy metals, achieving nearly 100% IQE and photoluminescence quantum yield (PLQY)—critical for high-performance OLEDs.[4−9] Moreover, TADF emitters enhance device lifetimes by facilitating reverse intersystem crossing (RISC), a thermally assisted transition of excitons from the T_1 to the singlet (S_1) state.

The efficiency of RISC depends on several molecular parameters: (1) a small singlet−triplet energy gap (ΔE_{ST} < 0.2 eV), (2) strong spin−orbit coupling (SOC), (3) high oscillator strength (f), and (4) minimal reorganization energy associated with transitions between interacting states.[10,11] Molecular design is pivotal in optimizing these parameters. TADF

Received: February 9, 2025
Revised: April 15, 2025
Accepted: May 17, 2025

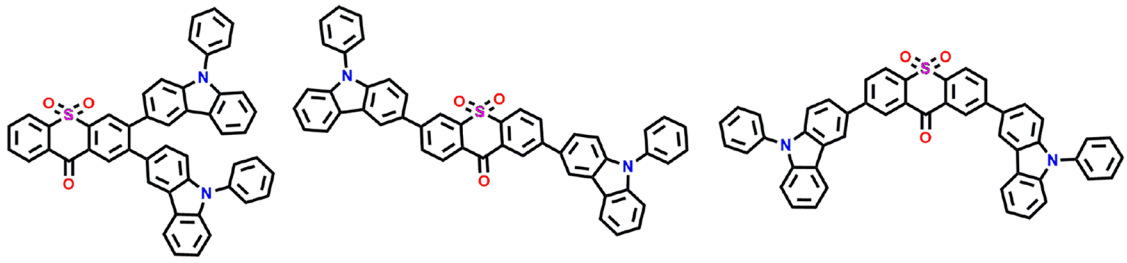

Figure 1. Chemical structures of the investigated D−A−D type TADF compounds in this work. The experimental details can be found in ref 38.

molecules typically feature spatially separated highest occupied molecular orbital (HOMO) and lowest unoccupied molecular orbital (LUMO), which minimizes ΔE_{ST} and facilitates efficient RISC. However, this spatial separation reduces *f*, creating a trade-off between ΔE_{ST} and *f*. Consequently, fine-tuning these properties through structural design is essential for achieving optimal performance.[12−23]

TADF emitters are broadly categorized into multiresonant (MR) and donor−acceptor (D−A−D or A−D−A) systems based on their molecular frameworks, significantly influencing their photophysical properties.[3,7−9] MR-TADF systems, characterized by rigid and planar structures, minimize vibrational flexibility and suppress nonradiative decay.[24−27] These systems typically incorporate fused aromatic rings with boron atoms as electron acceptors and heteroatoms (e.g., nitrogen, oxygen, sulfur) as donors. In contrast, D−A−D systems featuring donor and acceptor fragments connected by single bonds exhibit significant rotational motion. This flexibility increases the likelihood of nonradiative decay pathways by bringing conical intersection points (CIs) closer to the emitting S_1 state.[28,29] Consequently, D−A−D (or A−D−A) systems are more susceptible to conformational variations and nonradiative transitions, negatively impacting external quantum efficiency (EQE).[30]

Vibrational modes and molecular level insights[31] play a critical role in dictating radiative and nonradiative processes, with exciton-vibronic coupling or Herzberg−Teller (HT) coupling and Huang−Rhys (HR) factors being key determinants.[32,33] While MR-TADF systems benefit from structural rigidity that suppresses nonradiative decay, D−A−D systems require a comprehensive understanding of the interplay between structural dynamics and exciton-vibration coupling to optimize efficiency. Experimental techniques such as ultrafast and Raman vibrational spectroscopy have advanced our understanding of vibrational contributions to electronic transitions.[34−36] However, challenges remain in identifying vibrational modes that selectively promote radiative transitions or suppress nonradiative decay. Previous studies on Cu-based TADF complexes[33] and inverted ΔE_{ST} systems[29] have highlighted the importance of exciton-vibration coupling in facilitating or hindering transitions. Recent efforts to decouple excitons from high-frequency vibrational modes have provided valuable insights but have yet to fully address the contributions of specific vibrational modes to processes like internal conversion (IC), intersystem crossing (ISC), and RISC.[36,37]

This study investigates three D−A−D systems—2,3-TXP-PhCz, 2,6-TXP-PhCz, and 2,7-TXP-PhCz—to elucidate the impact of structural modifications on radiative and nonradiative pathways, focusing on vibrational mode analysis. Unlike earlier efforts, which primarily emphasized high-frequency vibrational modes or singular processes (RISC),[33,36] our work provides a holistic evaluation of all relevant transitions, including internal conversion, ISC, and RISC. By systematically analyzing conical intersection points and minimum energy crossing points (MECPs), we construct a detailed energy landscape that captures the interplay between Franck−Condon (FC) and adiabatic transitions across singlet and triplet states. Additionally, we extend the analysis to include low-frequency modes, which, despite their lower HR factors, play a significant role in modulating nonradiative processes due to their lower energy requirements. Our approach uniquely integrates Huang−Rhys factors, reorganization energies, and vibronic coupling calculations to quantify mode-specific contributions, distinguishing vibrational modes that enhance radiative rates from those that facilitate nonradiative decay. This comprehensive perspective validates computational predictions against experimental data and offers precise design principles for optimizing TADF emitters by balancing vibrational contributions to multiple processes. By addressing these gaps, our study provides actionable insights for the rational design of high-performance TADF emitters, setting it apart from prior investigations.

2. METHODS

In this study, we investigated three donor−acceptor−donor (D−A−D) type molecules—2,3-TXO-PhCz, 2,6-TXO-PhCz, and 2,7-TXO-PhCz—as illustrated in Figure 1. These molecules share identical molecular fragments, with the TXO fragment as the acceptor and the PhCz moiety as the donor. However, their primary distinction lies in the relative positions of the donor substituents on the TXO acceptor core.

The three investigated D−A−D emitters—2,3-TXP-PhCz, 2,6-TXP-PhCz, and 2,7-TXP-PhCz—were chosen due to their structural similarity yet markedly different photophysical behaviors. This contrast allows for a focused investigation of how subtle changes in molecular topology influence exciton dynamics and emission efficiency. Each molecule features a carbazole donor and a TXO acceptor, both of which are widely employed in high-performance OLED materials.[38−42] The well-documented relevance of these moieties in various molecular frameworks supports the generalizability of our findings. Thus, while the study focuses on a specific set of molecules, the conclusions drawn—particularly regarding the role of vibrational modes in modulating radiative and nonradiative processes—are expected to hold for a broader class of donor−acceptor systems.

While the experimental study[38] reported four TXO-based isomers, our computational investigation focused on three of them—2,3-TXP-PhCz, 2,6-TXP-PhCz, and 2,7-TXP-PhCz. The 3,6-isomer, despite exhibiting promising photophysical behavior and PLQY comparable to the efficient emitters in this series, was not included in our simulations due to the high computational cost associated with the complete vibrational-mode-resolved analysis. Our methodology requires geometry optimization and nonradiative decay rate

https://doi.org/10.1021/acsaelm.5c00286
ACS Appl. Electron. Mater. XXXX, XXX, XXX−XXX

Table 1. Electronic Properties of the Investigated D−A−D Molecules, Computed Using the PBE0/def2-TZVP Method[a]

molecule	S_1	S_2	T_1	T_2	λ	$\lambda_{Exp.}$
2,3-TXP-PhCz	2.08/2.66	2.16/2.90	1.85/2.46	2.27/2.80	597.42	574
2,6-TXP-PhCz	2.28/2.85	2.37/2.96	2.02/2.61	2.39/2.70	543.28	550
2,7-TXP-PhCz	2.24/2.83	2.38/2.88	2.05/2.66	2.05/2.72	554.61	550

[a]The table includes adiabatic (AD) and Franck-Condon (FC) transition energies for singlet (S_1, S_2) and triplet (T_1, T_2) states (in eV), as well as calculated (λ) and experimental ($\lambda_{Exp.}$) emission wavelengths (in nm). Transition energies are reported in the format AD/FC for clarity.

calculations for all 249 vibrational modes of each molecule, making the inclusion of an additional isomer significantly more demanding. To maintain both depth and feasibility, we selected a representative set that spans a range of emission efficiencies, allowing for a meaningful comparison of structure−property relationships.

In this study, we chose donor−acceptor−donor type molecules due to their inherent structural flexibility, allowing for rich vibrational dynamics. Unlike rigid multiresonance TADF systems, D−A−D architectures feature flexible single bonds between donor and acceptor units, enabling various conformational motions. This flexibility makes them particularly susceptible to nonradiative decay pathways such as internal conversion and intersystem crossing, thereby providing an ideal platform to investigate how specific vibrational modes influence photophysical processes.

The experimental synthesis and characterization of these compounds have been reported previously.[38] Despite their structural similarities, these molecules exhibit significant differences in key photophysical and device performance parameters, including photoluminescence quantum yield, exciton utilization efficiency, and external quantum efficiency (see Table S1). These differences highlight the critical influence of donor substitution patterns on the optoelectronic properties of D−A−D systems. This observation raises an important question: What molecular-level factors drive these variations in performance? To address this, we performed a detailed computational investigation focusing on the interplay between molecular structure, vibrational dynamics, and electronic transitions. By examining these aspects, we aim to uncover the underlying mechanisms that govern the optoelectronic behavior of these structurally related yet functionally distinct TADF systems.

All ground-state and excited-state geometry optimizations were conducted using the `Gaussian09` software,[43] with `GaussView` employed for structure visualization. Density Functional Theory (DFT) calculations utilized the PBE0 functional[44] in conjunction with the def2-TZVP basis set.[29,45] The ground-state geometries were first optimized, followed by frequency calculations at the same level of theory to confirm the absence of imaginary frequencies, thereby ensuring that the geometries correspond to true minima on the potential energy surface. These optimized ground-state geometries were used for single-point excited-state energy calculations, representing the vertical Franck−Condon energy states. Excited-state calculations were performed for the first singlet (S_1) and triplet (T_1) states, as well as the higher singlet (S_2) and triplet (T_2) states. Both vertical and adiabatic transition energies were computed to provide a comprehensive understanding of the electronic transitions. Crossing-point calculations were carried out using the `ORCA` program[46] to investigate nonadiabatic effects and their role in determining nonradiative decay pathways. Specifically, the conical intersection between the ground state (S_0) and the first excited singlet state (S_1) was analyzed. Minimum energy crossing point calculations were performed to identify intersections between excited singlet (S_1) and triplet (T_1) states. Finally, Hessian calculations for the ground-state and excited-state geometries (S_0, S_1, T_1) were performed, employing the same functional and basis set described above.

The parameters essential for understanding radiative and nonradiative processes, such as the Huang−Rhys factor and reorganization energy, were derived from frequency checkpoint files. The following equations describe the relationships governing the HR factor, vibrational coupling, and reorganization energies for each vibrational mode.

$$S_i(k) = \left[\frac{V_{ev(i)}(k)}{\hbar\omega_k}\right]^2 \tag{1}$$

Here, $S_i(k)$ represents the HR factor for a specific mode k, and ω_k is the frequency of the kth vibrational mode. These HR factors quantify the vibrational coupling for each mode. The vibrational reorganization energy, λ_ν, which measures the mode-specific contributions to electronic transitions, is related to the HR factors by

$$\lambda_\nu = \sum_k \hbar\omega_k S_i(k) \tag{2}$$

To calculate the exciton-vibration coupling for the excited electronic state i along each vibrational mode k, the following expression was used:

$$V_{ev(i)}(k) = \frac{E_{ex(i)}^{+\delta u_k} - E_{ex(i)}^{-\delta u_k}}{2\delta u_k} \tag{3}$$

Here δu_k is a small dimensionless displacement along the kth vibrational mode, and $E_{ex(i)}^{+\delta u_k}$ and $E_{ex(i)}^{-\delta u_k}$ are the excitation energies calculated for displacements $+\delta u_k$ and $-\delta u_k$, respectively, under the harmonic approximation. Using these parameters, the nonradiative rate (k_{nr}) was computed through the following rate equation.[36]

$$k_{nr} = \frac{C^2\sqrt{2\pi}}{\hbar\sqrt{\hbar\omega\Delta E}}\exp\left[-\frac{\Delta E}{\hbar\omega}\left\{\ln\left(\frac{\Delta E}{\sum_i \lambda_i}\right) - 1\right\}\right] \tag{4}$$

Here C is the effective electronic coupling matrix element, $\hbar$ is the reduced Planck constant, ω is the vibrational frequency of the accepting mode, ΔE is the energy gap between the initial and final states, and $\sum_i \lambda_i$ represents the total reorganization energy summed over all contributing vibrational modes. This methodology enabled the computation of mode-specific nonradiative rates while assessing the overall influence of vibrational modes on radiative and nonradiative processes.

To evaluate the overall impact of vibrations on rate constants, calculations were performed using `ORCA`, yielding rate constants along with the contributions of Franck−Condon and Herzberg−Teller terms as percentages. The significant contribution of HT terms underscores the importance of incorporating vibrational corrections in rate calculations (*vide infra*). Hessian files, crucial for these computations, were employed to determine fluorescence rates between the S_1 state and the ground state (S_0), as well as intersystem crossing rates. A sample input file for these calculations is provided in the Supporting Information (SI). For reverse intersystem crossing, the Marcus equation[47,48] was utilized. While the widely used Marcus equation provides a standard framework for rate predictions, our analysis revealed its limitations when applied to uncorrected spin−orbit coupling values. Reliable rate predictions were achieved by incorporating thermal correction factors, which account for vibrational contributions. Thus, the total SOC for the αth component (SOC_α) was calculated using[49]

$$SOC_\alpha = \sqrt{(SOC_\alpha)^2 + \sigma_\alpha^2} \tag{5}$$

where σ_α^2 accounts for the temperature-dependent vibrational correction to the αth SOC component and is defined as

https://doi.org/10.1021/acsaelm.5c00286
ACS Appl. Electron. Mater. XXXX, XXX, XXX−XXX

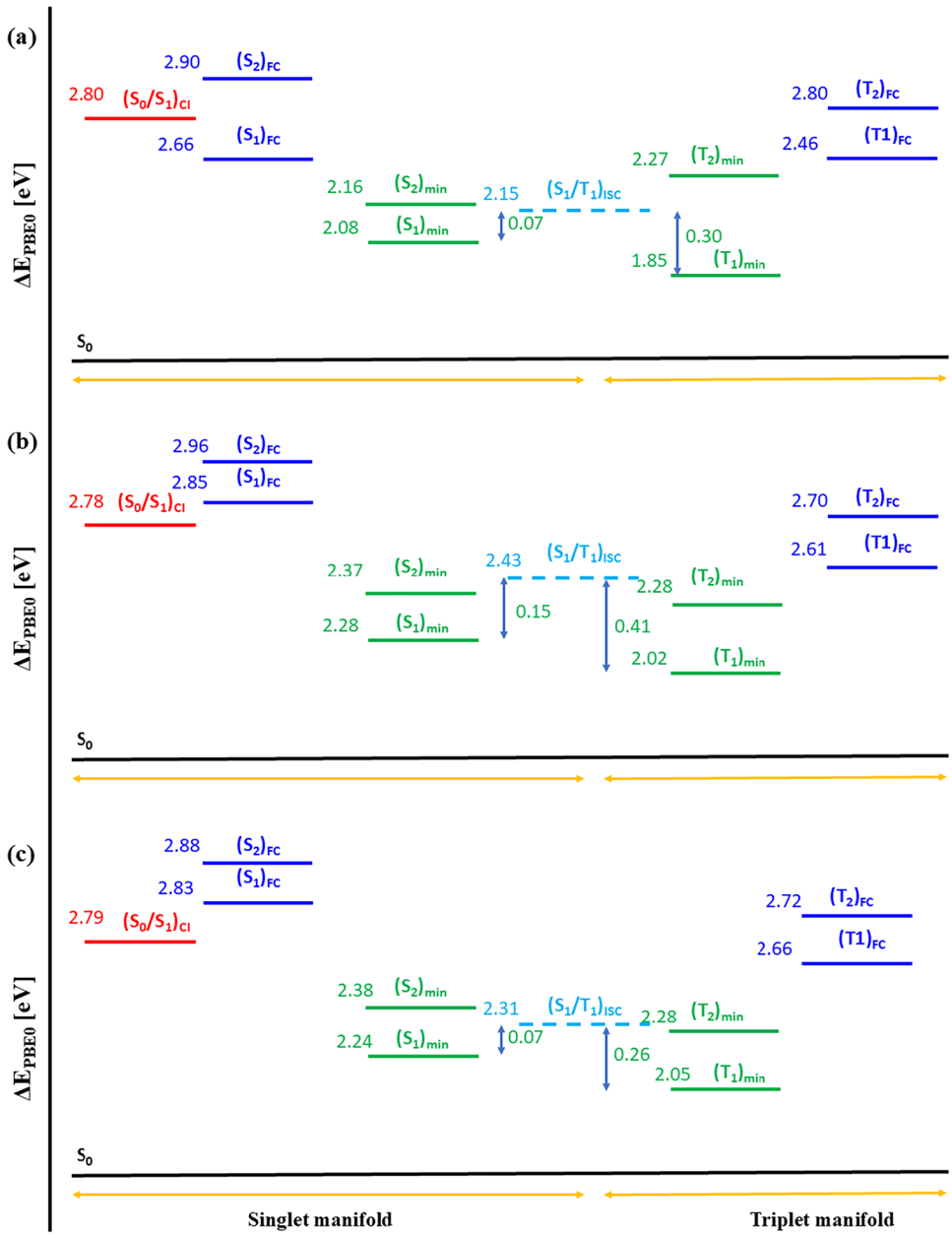

Figure 2. Energy landscapes (Jablonski diagram) of molecules 2,3-TXP-PhCz, 2,6-TXP-PhCz, and 2,7-TXP-PhCz, highlighting Franck−Condon energies (blue), adiabatic energies (green), conical intersection points (red), and minimum energy crossing points (cyan). Panels (a), (b), and (c) correspond to molecules 2,3-TXP-PhCz, 2,6-TXP-PhCz, and 2,7-TXP-PhCz, respectively, illustrating the key energy transitions and barriers relevant to singlet and triplet state dynamics.

$$\sigma_\alpha^2 = \sum_i^{3N-6} \frac{\hbar}{4\omega_i}\left(\frac{\partial \mathrm{SOC}_\alpha}{\partial Q_i}\right)^2 \cot h\left(\frac{\hbar\omega_i}{2k_B T}\right) \quad (6)$$

The summation extends over all $3N-6$ vibrational normal modes. ω_i is the frequency of the ith mode, Q_i denotes the displacement along the ith mode, T is the absolute temperature, $\hbar$ is the reduced Planck constant, and k_B is the Boltzmann constant.

3. RESULTS AND DISCUSSION

3.1. Energy Landscapes and Excited-State Dynamics.

The excitation energies of various electronic states and the corresponding emission wavelengths for the investigated molecules are summarized in Table 1. This table includes both adiabatic (AD) and Franck−Condon transition energies for the singlet (S_1, S_2) and triplet (T_1, T_2) states, calculated using the PBE0/def2-TZVP method. Additionally, the calculated emission wavelengths (λ) are compared with experimental values ($\lambda_{Exp.}$), providing a comprehensive evaluation of the computational approach. The data reveals excellent agreement between the calculated and experimental emission wavelengths, with 4 to 23 nm deviations. Among the three molecules, 2,3-TXP-PhCz exhibits the largest deviation (23 nm), while 2,7-TXP-PhCz shows the smallest deviation (~4 nm). These results validate the accuracy of the theoretical methods employed in this study for predicting optoelectronic properties. Additional experimental quantities and detailed comparisons are provided in Tables S1 and S2.

Significant differences are observed between the Franck−Condon and adiabatic energies for the investigated states, reflecting the structural relaxation following photoexcitation.

https://doi.org/10.1021/acsaelm.5c00286
ACS Appl. Electron. Mater. XXXX, XXX, XXX−XXX

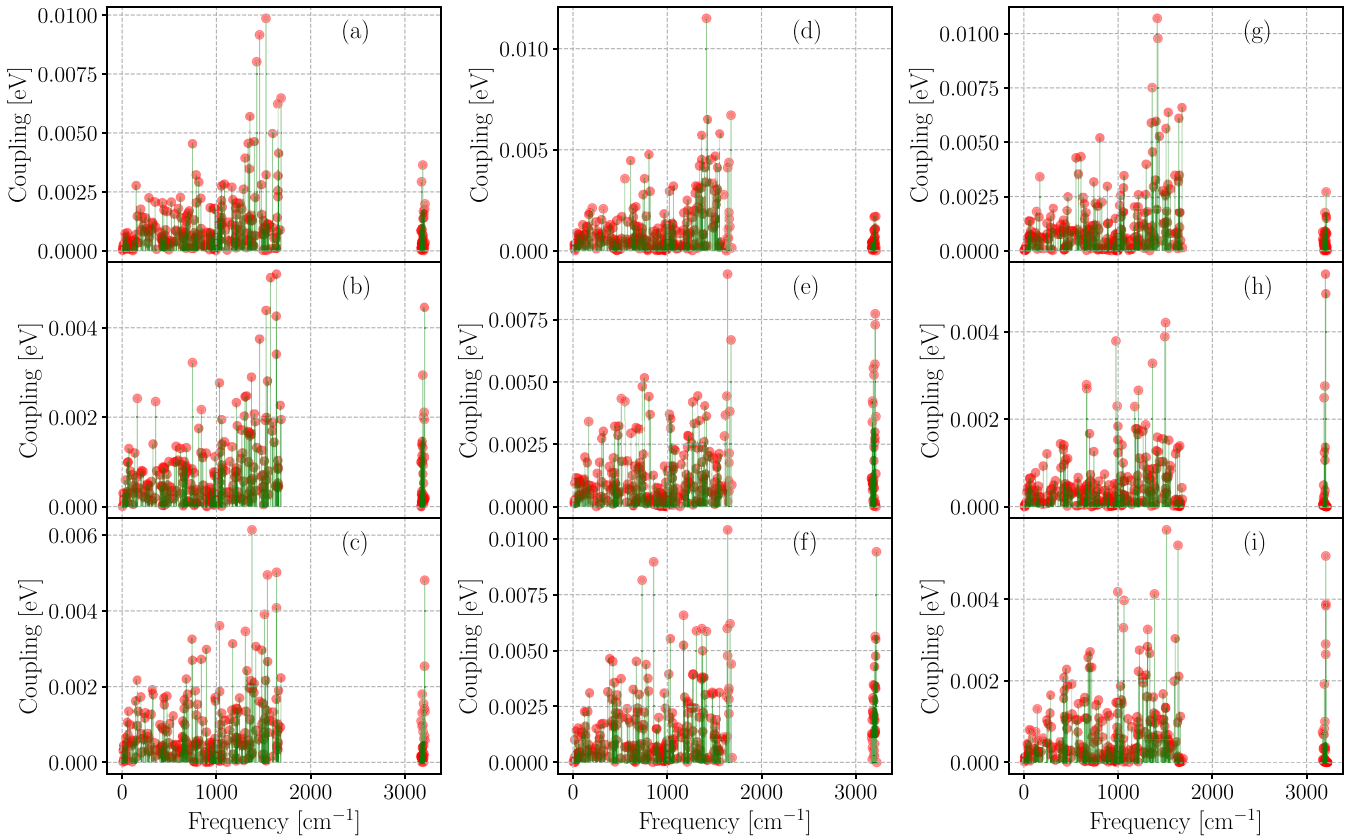

Figure 3. Exciton−phonon coupling strengths across low- and high-frequency vibrational modes for IC, ISC, and RISC transitions in 2,3-TXP-PhCz [left], 2,6-TXP-PhCz [middle], and 2,7-TXP-PhCz [right] molecules. Panels (a), (d), and (g) represent IC transitions; panels (b), (e), and (h) depict ISC transitions, and panels (c), (f), and (i) illustrate RISC transitions.

For instance, the energy difference for the S_1 state of molecule 2,3-TXP-PhCz is 0.58 eV, while for molecules 2,6-TXP-PhCz and 2,7-TXP-PhCz, these differences are 0.57 and 0.59 eV, respectively. The first adiabatic singlet excited state (S_1) is located at 2.08 eV for 2,3-TXP-PhCz, 2.28 eV for 2,6-TXP-PhCz, and 2.24 eV for 2,7-TXP-PhCz, indicating subtle variations in electronic structures across the molecules. Only the first two excited singlets (S_1 and S_2) and triplets (T_1 and T_2) are considered in this analysis, as higher-lying states contribute negligibly due to their increased energy gaps and reduced oscillator strengths, which render emissions from such states improbable.

To provide a comprehensive overview, the energy landscapes of the molecules are visualized in Figure 2, which incorporates critical conical intersection and minimum energy crossing point states. The Jablonski diagram divides the singlet and triplet manifolds, highlighting key energy transitions. Panels (a), (b), and (c) correspond to molecules 2,3-TXP-PhCz, 2,6-TXP-PhCz, and 2,7-TXP-PhCz, respectively. As shown in Figure 2, all adiabatic energies (green) lie below their corresponding FC energies (blue), consistent with Kasha's rule,[50] which predicts that vibrational relaxation occurs at the lowest vibrational state of the S_1 excited state following absorption. The energy gaps between the CI point and the S_1 state for 2,3-TXP-PhCz, 2,6-TXP-PhCz, and 2,7-TXP-PhCz are 0.72, 0.50, and 0.55 eV, respectively. These significant gaps suggest minimal interference of the CI with the lowest S_1 state, reducing the likelihood of nonradiative decay. This aligns with experimental observations, where nonradiative rates from the S_1 state range from 10^4 s^{-1} to 10^5 s^{-1}. Higher-energy state crossings with the ground state (S_0) are excluded, as they occur at significantly higher energy levels than the S_1−S_0 crossing.

The MECP crossings between S_1 and T_1 states, marked in cyan in Figure 2, play a crucial role in intersystem and reverse intersystem crossing. For ISC, the activation barriers for 2,3-TXP-PhCz, 2,6-TXP-PhCz, and 2,7-TXP-PhCz are 0.07, 0.15, and 0.07 eV, respectively. The corresponding activation barriers for RISC are 0.30, 0.41, and 0.26 eV. Notably, molecule 2,6-TXP-PhCz exhibits the highest ISC barrier (0.15 eV), which is advantageous as it limits the transition of excitons from S_1 to T_1, thereby retaining more excitons in the S_1 state. Conversely, 2,7-TXP-PhCz is the most favorable for RISC due to its lower activation energy (0.26 eV), facilitating the harvesting of excitons from the T_1 state. While activation energies provide valuable insights into ISC and RISC processes, it is essential to acknowledge that reorganization energies and electronic couplings also influence these transitions. These factors warrant further investigation to fully understand the dynamics of exciton transitions in these systems.

In addition, although the absolute dipole moments of the molecules in their ground and excited states do not directly correlate with their photoluminescence quantum yields, a noteworthy trend is observed in the change of dipole moment upon excitation. Among the three molecules, 2,3-TXP-PhCz shows the largest dipole moment change, followed by 2,6-TXP-PhCz and 2,7-TXP-PhCz, mirroring an inverse trend in their PLQYs. This suggests that a larger dipole moment change may be indicative of increased electronic reorganization and potentially enhanced nonradiative decay pathways such as

https://doi.org/10.1021/acsaelm.5c00286
ACS Appl. Electron. Mater. XXXX, XXX, XXX−XXX

internal conversion. Thus, while the static dipole moment alone may not dictate emission efficiency, the extent of dipole variation between electronic states can serve as a qualitative descriptor for exciton stability and emission performance. The corresponding dipole moment values have been compiled in Table S4.

3.2. Huang−Rhys Factor and Exciton−Phonon Coupling. The Huang−Rhys factors and vibronic couplings for each vibrational mode of the molecules under investigation were calculated using eqs 1 and 3. The total number of vibrational modes for nonlinear molecules is 3*N*-6, where *N* denotes the number of atoms in the molecule. In this study, all molecules consist of 85 atoms, resulting in 255 total modes, of which 249 correspond to vibrational modes. A frequency analysis reveals an absence of vibrational modes in the range of 1800 to 2800 cm^{-1} for these molecules. The vibrational modes were categorized into low- and high-frequency regions to facilitate the analysis. The low-frequency modes, spanning from mode 1 to mode 220, lie within the range of up to 1700 cm^{-1}, while the high-frequency modes, encompassing modes 221 to 249, are located between approximately 3000 and 3250 cm^{-1}. Figures S1 and S2 provide a detailed HR factor analysis for these modes.

The HR factor analysis highlights distinct trends. As shown in Figure S1, low-frequency modes exhibit significantly higher HR factors, indicating substantial molecular displacement and structural reorganization. In contrast, Figure S2 demonstrates that high-frequency modes have two to 3 orders of magnitude lower HR factors, suggesting minimal displacement and structural changes for these modes. This disparity underscores the dominant role of low-frequency modes in inducing large-scale molecular reorganization.[36] However, a deeper examination reveals that modes with HR factors exceeding 1 are typically delocalized in nature. Consequently, these modes are less effective at coupling with electronic transitions and have a limited contribution to nonradiative decay rates.[36] In contrast, despite their lower HR factors, high-frequency modes exhibit stronger exciton-vibration couplings. These couplings are more significant in driving nonradiative processes, making high-frequency modes critical to understanding and optimizing molecular photophysics.

The vibrational exciton−phonon coupling across different transitions is summarized in Figure 3, which comprehensively compares low- and high-frequency modes. Each panel in the figure corresponds to a specific molecule and transition type: panels (a), (d), and (g) represent the IC transitions for 2,3-TXP-PhCz, 2,6-TXP-PhCz, and 2,7-TXP-PhCz molecules, respectively; panels (b), (e), and (h) depict the ISC transitions; and panels (c), (f), and (i) highlight the RISC transitions. The data reveal intriguing patterns in the coupling strengths. Low-frequency modes (below 1700 cm^{-1}) dominate the IC transitions, exhibiting significantly stronger exciton−phonon couplings than ISC and RISC processes. This is particularly evident in the 2,3-TXP-PhCz molecule (panel a), where a high density of strongly coupled modes suggests extensive molecular reorganization during the IC process. Conversely, for ISC and RISC transitions, high-frequency modes play a significant role in exciton−phonon coupling, as evidenced in panels (e, f) and (h), (i), where pronounced coupling is observed for the 2,6-TXP-PhCz and 2,7-TXP-PhCz molecules in these regions. Interestingly, the middle-frequency modes (∼1700 cm^{-1}) emerge as pivotal contributors to coupling strength across all transitions, except for panel (h), where the high-frequency modes dominate the ISC process for the 2,7-TXP-PhCz molecule. Overall vibrational modes below 500 cm^{-1} typically correspond to low-frequency bending motions, often involving out-of-plane deformations and collective skeletal displacements of the molecular framework. These modes are energetically less demanding and play an important role in structural reorganization. Modes in the 500−1000 cm^{-1} range exhibit mixed character, combining in-plane and out-of-plane displacements, particularly hydrogen and heavier atoms such as carbon and oxygen within the conjugated rings. Notably, the modes in the 1200−1700 cm^{-1} range predominantly involve C═C stretching vibrations and associated in-plane motions. These modes exhibit the strongest exciton−phonon coupling and are consistently found to contribute significantly to nonradiative electronic transitions, including internal conversion, intersystem, and reverse intersystem crossing.

To elucidate their roles, we have identified the key vibrational modes that dominate each relaxation process for the three molecules studied. In IC, the most strongly coupled modes are the 219th, 218th, and 218th for molecules 2,3-TXP-PhCz, 2,6-TXP-PhCz, and 2,7-TXP-PhCz, respectively, all located near 1678 cm^{-1}. For ISC, the dominant contributions arise from the 211th mode (approximately 1640 cm^{-1}) in both 2,3-TXP-PhCz and 2,6-TXP-PhCz, while for 2,7-TXP-PhCz, the 237th mode around 3200 cm^{-1}—likely associated with N−H stretching—plays a significant role. In the case of RISC, the 212th, 217th, and 197th modes are most critical for 2,3-TXP-PhCz, 2,6-TXP-PhCz, and 2,7-TXP-PhCz, respectively, with corresponding frequencies of approximately 1640, 1660, and 1514 cm^{-1}. These results underscore the importance of specific vibrations in mediating exciton−phonon interactions and their varying influence depending on the nature of the transition.

The observed preference for low-frequency modes in internal conversion and high-frequency modes in intersystem crossing and reverse ISC reflects the fundamental differences in their mechanisms. IC involves nonradiative relaxation between states of the same spin multiplicity (e.g., $S_1 \rightarrow S_0$), where low-frequency modes (typically below 500 cm^{-1}) such as torsional and out-of-plane bending motions dominate due to their strong vibronic coupling and ability to facilitate structural reorganization and energy dissipation. These modes enhance the Franck−Condon overlap and are well-suited for bridging small energy gaps. In contrast, ISC and RISC are spin-forbidden transitions between states of different spin multiplicities, which require spin−orbit coupling. Here, high-frequency modes become important as they modulate electronic distributions and orbital character via Herzberg−Teller coupling, enhancing SOC and enabling efficient spin-flip processes. This behavior is consistent with El-Sayed's rule[51] and has been reported in several π-conjugated systems, e.g., nonfullerene acceptors.[52] Among the three molecules, the 2,3-TXP-PhCz molecule exhibits the highest number of strongly coupled vibrational modes for IC transitions, as highlighted by the dense cluster of red points with green lines in panel (a). This strong coupling facilitates nonradiative decay, reducing photoluminescence quantum yield by promoting energy loss from the S_1 state. In contrast, the 2,6-TXP-PhCz molecule displays minimal coupling in high-frequency modes for IC transitions (panel d), indicating a reduced contribution to nonradiative rates and improved PLQY.

For ISC transitions, the coupling trends shift dramatically. The 2,6-TXP-PhCz molecule (panel e) exhibits the strongest

https://doi.org/10.1021/acsaelm.5c00286
ACS Appl. Electron. Mater. XXXX, XXX, XXX−XXX

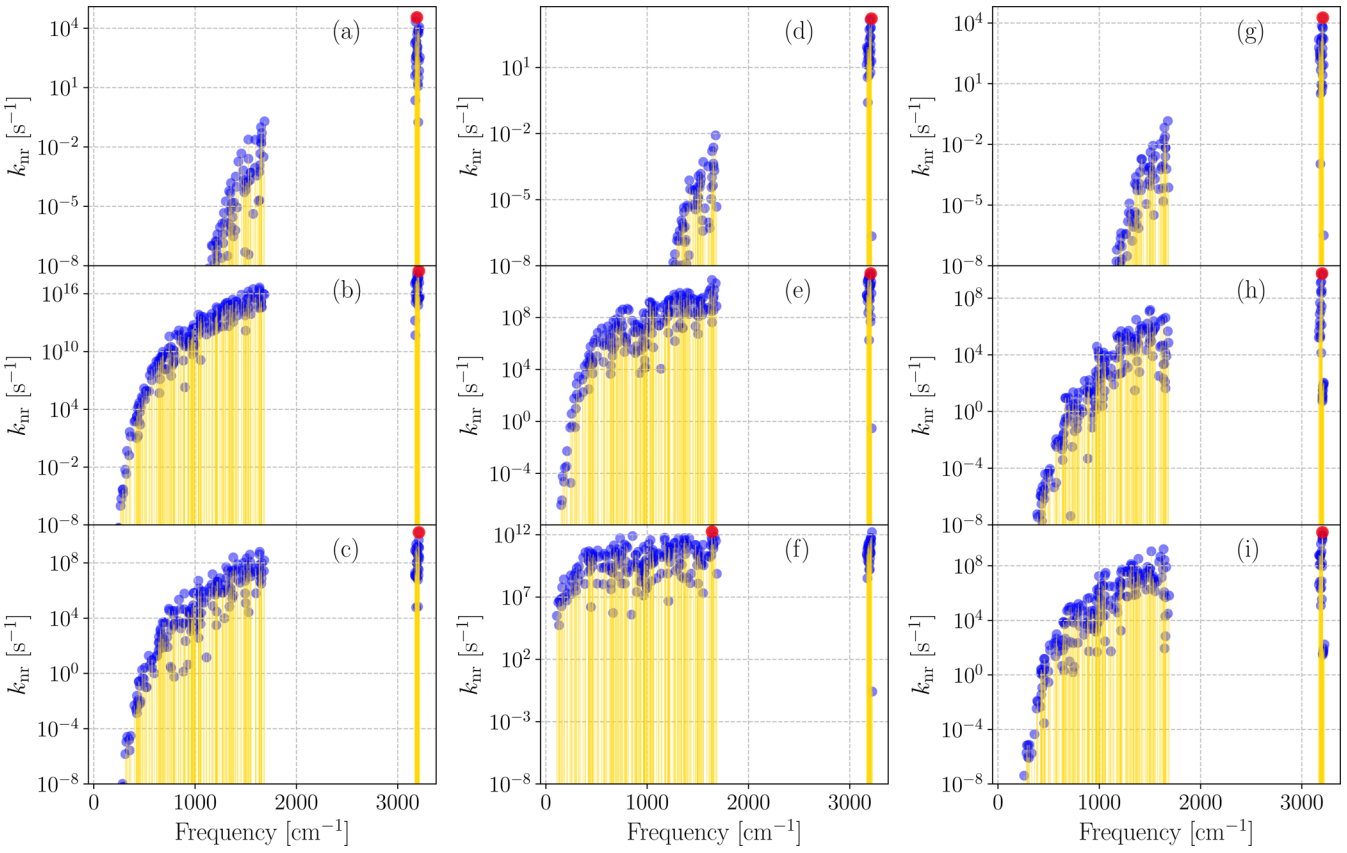

Figure 4. Vibrational mode contributions to nonradiative rates for (a, d, g) internal conversion (IC), (b, e, h) intersystem crossing (ISC), and (c, f, i) reverse intersystem crossing (RISC) transitions in molecules 2,3-TXP-PhCz [left], 2,6-TXP-PhCz [middle], and 2,7-TXP-PhCz [right], respectively. The red dots indicate the mode with the highest contribution for each process in these molecules.

exciton−phonon couplings, followed by comparable values for the 2,3-TXP-PhCz (panel b) and 2,7-TXP-PhCz (panel h) molecules. This suggests that the vibrational modes in the 2,6-TXP-PhCz molecule are more effective at supporting the ISC process, potentially facilitating efficient intersystem crossing. Similarly, the RISC process is most strongly coupled in the 2,6-TXP-PhCz molecule (panel f), with moderate couplings in the 2,3-TXP-PhCz and 2,7-TXP-PhCz molecules (panels c and i). These trends underline the 2,6-TXP-PhCz molecule's ability to leverage vibrational modes for efficient reverse intersystem crossing, contributing to higher exciton utilization. The balance of exciton−phonon coupling across transitions is critical for overall efficiency. While the 2,3-TXP-PhCz molecule suffers from strong IC coupling that undermines PLQY, the 2,6-TXP-PhCz molecule excels in ISC and RISC processes, achieving superior exciton utilization. The 2,7-TXP-PhCz molecule strikes a middle ground, with moderate coupling across transitions and reduced IC coupling, resulting in improved efficiency compared to the 2,3-TXP-PhCz molecule. These findings highlight the subtle interplay between vibrational modes and electronic transitions, offering insights into designing emitters with optimized photophysical properties.

3.3. Nonradiative Rates. We examined electron−phonon coupling and its influence on specific transitions in the preceding discussion. However, these couplings alone do not fully dictate transition rates. Additional factors, such as vibrational frequencies, energy gaps between electronic states, and reorganization energies, collectively shape the dynamics of these processes. To capture these effects comprehensively, we calculated the nonradiative rates using eq 4, which integrates all relevant contributions under the assumption of weak coupling. These rates, which directly correlate with the molecule's photophysical properties, such as PLQY and EQE, are illustrated in Figure 4.

The results highlight that high-frequency vibrational modes predominantly contribute to nonradiative rates for intersystem crossing, reverse intersystem crossing, and internal conversion transitions. Analyzing each transition in detail, we observe that for IC (Figure 4a−d−g), the 2,3-TXP-PhCz molecule shows the most substantial contributions, with some vibrational modes exceeding 10^4 s^{-1}, whereas 2,6-TXP-PhCz and 2,7-TXP-PhCz show moderate contributions, with 2,7-TXP-PhCz slightly surpassing 2,6-TXP-PhCz. For the ISC process, as shown in Figure 4b−e−h, the contribution of vibrational modes to ISC is the highest for 2,3-TXP-PhCz molecule. Some modes even exhibit contributions exceeding 10^{16} s^{-1}, indicating strong support for the ISC transition in the case of 2,3-TXP-PhCz. For the 2,6-TXP-PhCz molecule, a more significant number of modes contribute within the range of 10^8 to 10^{12} s^{-1} compared to the 2,7-TXP-PhCz molecule, suggesting that 2,6-TXP-PhCz has a higher overall contribution to ISC compared to 2,7-TXP-PhCz. In the case of RISC (Figure 4c−f−i), 2,3-TXP-PhCz exhibits the weakest contributions, while 2,6-TXP-PhCz shows the strongest, particularly with the 218th vibrational mode at 1678 cm^{-1} dominating the rates. The 2,7-TXP-PhCz molecule demonstrates contributions greater than 2,3-TXP-PhCz but fewer than 2,6-TXP-PhCz.

These findings align with experimental observations (Table S1). For IC and ISC transitions, which benefit from the absence of promoting vibrational modes to enhance exciton

https://doi.org/10.1021/acsaelm.5c00286
ACS Appl. Electron. Mater. XXXX, XXX, XXX−XXX

utilization efficiency, 2,3-TXP-PhCz exhibits the highest vibrational contributions, correlating with its lowest PLQY (62%) and EQE (12%). On the other hand, 2,6-TXP-PhCz and 2,7-TXP-PhCz exhibit comparable IC contributions, but 2,6-TXP-PhCz shows stronger ISC and RISC support. Despite weaker RISC contributions, 2,7-TXP-PhCz achieves the highest PLQY due to its reduced ISC and higher oscillator strength (Table S2) for the emissive transition. Consequently, 2,7-TXP-PhCz emerges as the most efficient molecule, followed by 2,6-TXP-PhCz, and finally 2,3-TXP-PhCz, with PLQY of 89, 83.8, and 62.1%, respectively. This comprehensive analysis underscores the intricate interplay of vibrational modes and nonradiative transitions in determining the photophysical performance of these molecules.

We emphasize the interplay between radiative and nonradiative processes to provide a holistic picture of the factors governing photoluminescence quantum yield. Vibrational modes play a dual role: while they can enhance undesirable nonradiative pathways such as internal conversion and intersystem crossing, they can also facilitate reverse intersystem crossing, which positively contributes to delayed fluorescence. Among the studied compounds, 2,3-TXP-PhCz exhibits strong vibrational support for both IC and ISC, resulting in the lowest PLQY. In contrast, 2,6-TXP-PhCz and 2,7-TXP-PhCz display reduced support for these loss pathways. However, 2,6-TXP-PhCz suffers from a higher ISC rate due to larger spin−orbit coupling, leading to increased triplet loss. This makes 2,7-TXP-PhCz the most efficient emitter, achieving the highest PLQY due to minimized nonradiative losses and a favorable balance of radiative and RISC processes. This analysis underscores the importance of vibrational mode engineering in optimizing exciton dynamics for high-efficiency TADF emitters.

3.4. Exciton Characteristics. In earlier discussions, we examined the influence of individual vibrational modes on exciton−phonon coupling and their contributions to nonradiative decay rates. It is important to note that the calculated internal conversion rates correspond to specific vibrational contributions rather than the total IC rates, as not all vibrational modes contribute equally or simultaneously to these transitions. Consequently, the actual IC rates are lower than the cumulative contributions from all modes. Therefore, analyzing the coupling or decoupling behavior of specific vibrational modes is critical, as these interactions significantly impact molecular performance. The nature of the participating orbitals primarily determines the coupling or decoupling of vibrational modes from electronic transitions. Effective decoupling requires both the HOMO and LUMO to be spatially and energetically separated from vibrational motion. To investigate these interactions, we analyzed the S_1 to S_0 transition, focusing on the HOMO, LUMO, and their alignment with the molecular vibrational plane. As shown in Table 2, nearly 100% of the S_1 to S_0 transition occurs via the HOMO-to-LUMO pathway across all molecules. The HOMO exhibits a nonbonding character associated with oxygen atom lone pairs, oriented outside the molecular vibrational plane, facilitating decoupling from vibrational motion.[36] In contrast, the LUMO displays an antibonding π planar character, making it more challenging to decouple from vibrations. This shared orbital characteristic across all molecules explains their low nonradiative IC rates, consistent with experimental observations in the range of 10^4−10^5 s^{-1}. Most vibrational modes are effectively decoupled from the HOMO but may still couple with the LUMO, aligning with the observed trends.

Table 2. Exciton Characteristics of the Studied Molecules, Including the Percentage Contribution of HOMO-to-LUMO Transitions, the Type of Electronic Transition, and the Ratio of the Vibrational Reorganization Energy (ϕ)[a]

molecule	HOMO to LUMO (%)	type	ϕ
2,3-TXP-PhCz	97.2	$n \rightarrow \pi^*$	0.0158
2,6-TXP-PhCz	97.3	$n \rightarrow \pi^*$	0.0042
2,7-TXP-PhCz	98.6	$n \rightarrow \pi^*$	0.0057

[a]ϕ represents the ratio of reorganization energies contributed by high-frequency modes (221−249) to low-frequency modes (1−220).

To further obtain a mode-resolved picture, we computed the ratio of the vibrational reorganization energy (ϕ) associated with all high-frequency normal modes (above 2000 cm^{-1}) to the low-frequency modes (100−1700 cm^{-1}) for a particular electronic transition. The ratio of reorganization energy was computed using the following equation.[53]

$$\phi = \frac{\sum_{k=2000\ cm^{-1}}^{3300\ cm^{-1}} \hbar\omega_k S_i(k)}{\sum_{k=100\ cm^{-1}}^{1700\ cm^{-1}} \hbar\omega_k S_i(k)} \quad (7)$$

As evident from Table 2, among the molecules, 2,3-TXP-PhCz exhibits the highest reorganization energy ratio, indicating a more significant contribution of high-frequency modes to its electronic transitions compared to 2,6-TXP-PhCz and 2,7-TXP-PhCz. This stronger exciton−phonon coupling for 2,3-TXP-PhCz aligns with its lower photoluminescence quantum yield obtained from the experiment, as shown in Table S1.

To understand how vibrational modes influence electronic transitions, we analyzed the exciton wave function (ρ) and its change ($\Delta\rho$) due to displacements along specific vibrational modes. This analysis focused on the vibrational mode that contributes most significantly to internal conversion, primarily associated with the C−H vibrations of the benzene rings. The displacement directions of these modes are depicted in the first row of Figure 5, while the second and third rows represent the computed exciton wave function (ρ) and its change ($\Delta\rho$), respectively. The computed wave function (ρ) highlights the delocalized nature of the S_1 exciton across the molecular framework, exhibiting a charge-transfer character. The change in the wave function ($\Delta\rho$), shown in the third row, reveals how the electronic structure responds to displacements along the vibrational mode. A significant $\Delta\rho$ indicates a strong coupling between the vibrational mode and the electronic transitions.[36] Among the three molecules, 2,6-TXP-PhCz exhibits the smallest $\Delta\rho$, indicating the most effective decoupling of vibrations from electronic transitions, followed by 2,7-TXP-PhCz and 2,3-TXP-PhCz, a similar pattern seen from Figures 3 and 4. This trend aligns with experimentally observed nonradiative rate constants, which are relatively low ($\sim 10^4$ s^{-1}) and underscores the importance of vibrational decoupling in minimizing nonradiative decay rates. These findings provide valuable insights into molecular design strategies that target vibrational modes to suppress nonradiative transitions and optimize exciton utilization efficiency.

3.5. Vibronic Assisted Spin−Orbit Couplings. Traditional approaches, such as the classical Marcus rate equations, often neglect vibrational contributions, leading to significant discrepancies between theoretical predictions and experimental observations. The necessity of including vibrational corrections becomes evident when uncorrected SOC values are used in the Marcus equation (eqs S1−S2). Without these corrections, the

https://doi.org/10.1021/acsaelm.5c00286
ACS Appl. Electron. Mater. XXXX, XXX, XXX−XXX

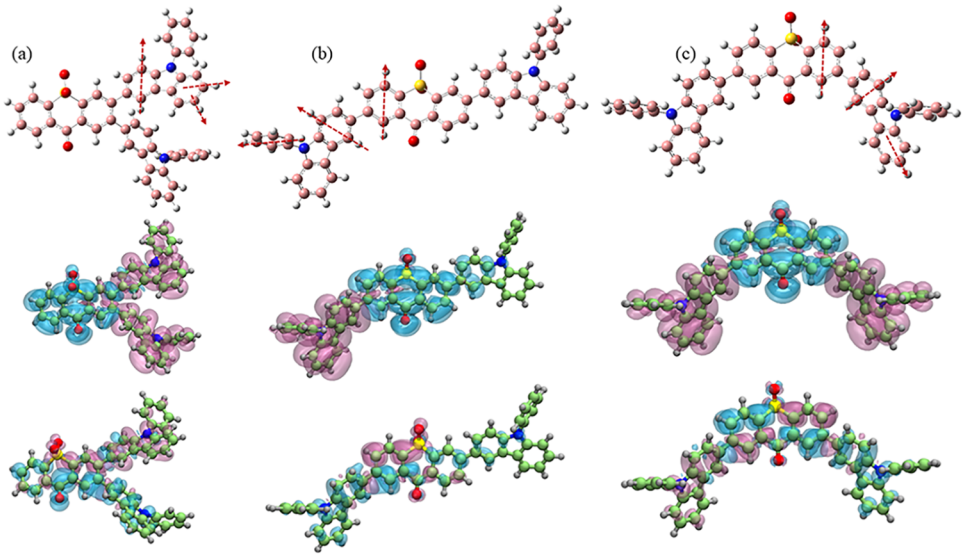

Figure 5. Visualization of the highest-contributing vibrational modes for internal conversion transitions in the investigated molecules: (a) 2,3-TXP-PhCz, (b) 2,6-TXP-PhCz, and (c) 2,7-TXP-PhCz. The first row highlights the vibrational modes, with red arrows indicating the direction and magnitude of the vibrational motion. The second row shows the wave function plots, illustrating charge transfer behavior, while the third row presents the differential wave function plots, demonstrating the changes in wave function upon vibrational displacement.

resulting rate constants are unrealistically low, underscoring the critical role of vibrational effects. Table S3 shows that HT contributions dominate over FC terms, emphasizing the importance of incorporating HT terms when calculating rate constants. The spin−orbit coupling corrections were performed at the same level of the theory described in Section 2, employing the PBE0 functional and the def2-TZVP basis set. Starting from the optimized ground-state geometry, we carried out a mode-specific displacement along each vibrational normal coordinate (Q_i) and computed the corresponding SOC values at several points along this coordinate. The slope $\partial(\mathrm{SOC})/\partial Q_i$ was then extracted to quantify how the SOC varies with nuclear motion. This derivative was used in eq 6 to calculate the mode-resolved correction factors. The corrected SOC values were subsequently obtained by incorporating these factors into the initially computed SOCs, as described in eq 5. This procedure accounts for both electronic and vibrational contributions to SOC, offering a more accurate representation of spin-vibronic coupling. To highlight the significance of these corrections, we have included both the corrected and uncorrected SOC values in Tables S2 and S4. The corrected SOC values and the resulting rates, summarized in Table S2, demonstrate that vibrational corrections yield physically meaningful results.

Figure 6 illustrates the temperature-dependent behavior of SOC values (see eqs 5 and 6), showing a consistent increase with rising temperature across all molecules. Among the studied compounds, 2,6-TXP-PhCz exhibits the highest SOC values, followed by 2,3-TXP-PhCz and. These corrected SOC values lead to computed rates that align well with experimental data, as shown in Tables S1 and S2. Moreover, all rates fall within a single order of magnitude, as depicted in Figure S3. A notable discrepancy arises in the computed ISC rate for 2,7-TXP-PhCz, which is significantly higher than the experimental value. This difference can be attributed to the computed ΔE_{ST} for 2,7-TXP-PhCz, which is approximately 20 times larger than the experimental value (see Tables S1 and S2). Interestingly, all three molecules of identical molecular core and building

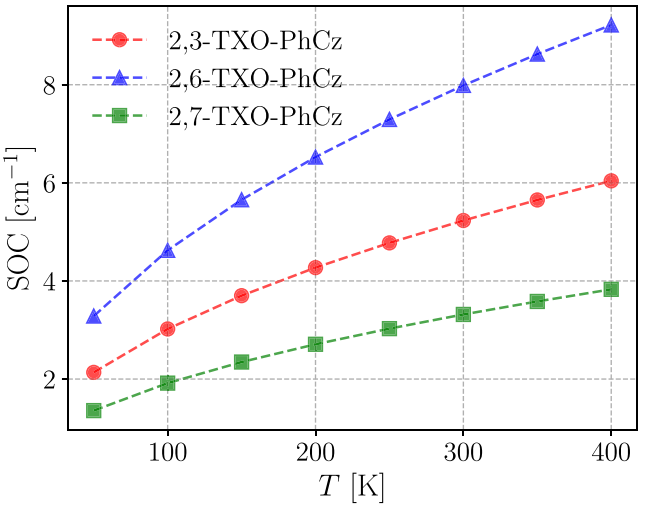

Figure 6. Temperature-dependent total spin−orbit coupling (SOC) for the investigated molecules, illustrating the variation in SOC values with temperature.

blocks exhibit similar ΔE_{ST} gaps in the computed results. This suggests that the experimental determination of the S_1-T_1 gap for 2,7-TXP-PhCz may involve uncertainties or variations, possibly due to experimental conditions or measurement limitations. While the B3LYP/6−31G(d,p) level of theory was used in the original experimental study,[38] it exhibited inconsistent performance across the molecular series, significantly underestimating ΔE_{ST} for several emitters. Consequently, we adopted the PBE0 functional, which provides a more balanced and reliable description of excited-state energetics across this class of molecules and has also been validated in recent literature.[29] Although PBE0 still slightly overestimates ΔE_{ST} for the 2,7 isomer, it improves overall agreement with experimental data for the rest of the series. Incorporating more accurate, albeit computationally expensive, methods—such as optimally tuned range-separated hybrids or double-hybrid functionals—could further refine this predic-

https://doi.org/10.1021/acsaelm.5c00286
ACS Appl. Electron. Mater. XXXX, XXX, XXX−XXX

tion, and future work employing such higher-level approaches may offer improved quantitative accuracy, especially for systems with subtle electronic structure variations. Although 2,6-TXP-PhCz exhibits the highest activation barrier for ISC, its rate remains comparatively high due to its significantly larger spin−orbit coupling (Table S2), highlighting that ISC is influenced by both the barrier height and the magnitude of spin−orbit interactions. Incorporating vibrational corrections into SOC calculations and the Marcus equation has provided significant insights into ISC and RISC processes. These corrections not only improve the accuracy of rate constants but also ensure their physical relevance, highlighting the critical role of vibrational effects in understanding and optimizing molecular photophysical properties.

The insights gained from our vibrational mode analysis offer a practical design strategy for developing new high-efficiency emitters. One can predict the exciton dynamics of new candidate molecules by identifying vibrational modes that predominantly enhance nonradiative decay processes such as ISC and IC or, alternatively, support radiative mechanisms like RISC. Molecules can then be rationally modified—for instance, by introducing structural rigidity or altering donor−acceptor configurations—to suppress deleterious modes while preserving or enhancing beneficial ones. This framework thus enables targeted molecular design aimed at maximizing photoluminescence quantum yield and overall emission performance.

Although this study focuses on a specific set of D−A−D type emitters, the computational framework developed herein is general and can be readily extended to conventional donor−acceptor systems. The formalism relies on vibrational mode-resolved analysis of spin-allowed and spin-forbidden transitions, which are inherent to all organic emitters. As such, the insights gained from quantifying mode-specific contributions to radiative and nonradiative processes, including ISC and RISC, apply to a broader class of TADF materials. We anticipate that this methodology can serve as a valuable tool for exploring structure−property relationships in diverse molecular backbones beyond the specific architectures studied here.

4. CONCLUSIONS

This study elucidates the intricate interplay between vibrational and electronic properties in three donor−acceptor−donor (D−A−D) type molecules—2,3-TXP-PhCz, 2,6-TXP-PhCz, and 2,7-TXP-PhCz—to uncover the factors governing their photophysical performance. Despite structural similarities, these molecules exhibit markedly different photoluminescence quantum yields and external quantum efficiencies. Our analysis reveals that these variations arise from the distinct roles of vibrational modes in facilitating or suppressing radiative and nonradiative processes. By integrating vibrational corrections into spin−orbit coupling calculations and incorporating these corrections into the Marcus theory, we achieved accurate predictions of intersystem crossing and reverse intersystem crossing rates. The methodology provided deeper insights into the critical influence of vibrational contributions on exciton dynamics. Furthermore, exciton wave function (ρ) and its change ($\Delta\rho$) highlighted the extent of vibrational mode decoupling, demonstrating how specific modes influence internal conversion while minimizing overall nonradiative energy losses. These findings underscore the importance of balancing vibrational and electronic factors to optimize exciton utilization efficiency in thermally activated delayed fluorescence emitters. Our study provides a robust framework for the rational design of high-performance OLED materials, offering actionable strategies to enhance device efficiency by targeting key vibrational modes and electronic transitions.[36] This work paves the way for future advancements in TADF emitter design, bridging the gap between theoretical predictions and experimental realizations for next-generation optoelectronic applications.

■ ASSOCIATED CONTENT

Data Availability Statement

The data that support the findings of this study are available from the corresponding authors upon reasonable request.

Supporting Information

The Supporting Information is available free of charge at https://pubs.acs.org/doi/10.1021/acsaelm.5c00286.

Description to determine photophysical rates, Huang−Rhys factors, and tables of photophysical data (PDF)
Geometries (ZIP)

■ AUTHOR INFORMATION

Corresponding Author

Anirban Mondal − *Department of Chemistry, Indian Institute of Technology Gandhinagar, Gandhinagar, Gujarat 382355, India;* orcid.org/0000-0003-3029-8840; Email: amondal@iitgn.ac.in

Author

Sanyam − *Department of Chemistry, Indian Institute of Technology Gandhinagar, Gandhinagar, Gujarat 382355, India;* orcid.org/0000-0001-7410-8207

Complete contact information is available at: https://pubs.acs.org/10.1021/acsaelm.5c00286

Author Contributions

A.M. conceived the problem. Sanyam conducted all the simulations. Sanyam and A.M. analyzed the results and prepared the draft.

Notes

The authors declare no competing financial interest.

■ ACKNOWLEDGMENTS

The authors gratefully acknowledge the Indian Institute of Technology Gandhinagar, India, for providing research facilities and financial support. Sanyam thanks CSIR for the fellowship. We thank PARAM Ananta for computational resources. We are grateful to Dr. Partha Pratim Roy for helpful discussions and critical reading of our manuscript.

■ REFERENCES

(1) Endo, A.; Sato, K.; Yoshimura, K.; Kai, T.; Kawada, A.; Miyazaki, H.; Adachi, C. Efficient up-conversion of triplet excitons into a singlet state and its application for organic light emitting diodes. *Appl. Phys. Lett.* **2011**, *98*, No. 083302.

(2) Liu, Y.; Li, C.; Ren, Z.; Yan, S.; Bryce, M. R. All-organic thermally activated delayed fluorescence materials for organic light-emitting diodes. *Nat. Rev. Mater.* **2018**, *3*, No. 18020.

(3) Uoyama, H.; Goushi, K.; Shizu, K.; Nomura, H.; Adachi, C. Highly efficient organic light-emitting diodes from delayed fluorescence. *Nature* **2012**, *492*, 234−238.

(4) Xu, Y.; Cheng, Z.; Li, Z.; Liang, B.; Wang, J.; Wei, J.; Zhang, Z.; Wang, Y. Molecular-structure and device-configuration optimizations toward highly efficient green electroluminescence with narrowband

emission and high color purity. *Adv. Opt. Mater.* **2020**, *8*, No. 1902142.
(5) Xu, Y.; Li, C.; Li, Z.; Wang, Q.; Cai, X.; Wei, J.; Wang, Y. Constructing Charge-Transfer Excited States Based on Frontier Molecular Orbital Engineering: Narrowband Green Electroluminescence with High Color Purity and Efficiency. *Angew. Chem., Int. Ed.* **2020**, *59*, 17442−17446.
(6) Izumi, S.; Higginbotham, H. F.; Nyga, A.; Stachelek, P.; Tohnai, N.; Silva, Pd.; Data, P.; Takeda, Y.; Minakata, S. Thermally activated delayed fluorescent donor−acceptor−donor−acceptor π-conjugated macrocycle for organic light-emitting diodes. *J. Am. Chem. Soc.* **2020**, *142*, 1482−1491.
(7) Goushi, K.; Yoshida, K.; Sato, K.; Adachi, C. Organic light-emitting diodes employing efficient reverse intersystem crossing for triplet-to-singlet state conversion. *Nat. Photonics* **2012**, *6*, 253−258.
(8) Stachelek, P.; Ward, J. S.; dos Santos, P. L.; Danos, A.; Colella, M.; Haase, N.; Raynes, S. J.; Batsanov, A. S.; Bryce, M. R.; Monkman, A. P. Molecular Design Strategies for Color Tuning of Blue TADF Emitters. *ACS Appl. Mater. Interfaces* **2019**, *11*, 27125−27133.
(9) Zhang, Y.; Zhang, D.; Wei, J.; Hong, X.; Lu, Y.; Hu, D.; Li, G.; Liu, Z.; Chen, Y.; Duan, L. Achieving pure green electroluminescence with CIEy of 0.69 and EQE of 28.2% from an aza-fused multi-resonance emitter. *Angew. Chem.* **2020**, *132*, 17652−17656.
(10) Dos Santos, J. M.; Hall, D.; Basumatary, B.; Bryden, M.; Chen, D.; Choudhary, P.; Comerford, T.; Crovini, E.; Danos, A.; De, J.; Diesing, S.; Mahni, F.; Máire, G.; Abhishek, G. K.; Hassan, H.; Lea, H.; Emily, H.; Janine, H.; Tabea, H.; Durai, K.; Shiv, K.; Oliver, L.; Haoyang, L.; Fabien, L.; Ross, M. C. F.; Aminata, M.; Tomas, M.; Francis, M.; Yoann, O.; Quan, Q.; W, S. I. D.; Nidhi, S.; Changfeng, S.; Leander, S.; Pagidi, S.; Dianming, S.; Eglè, T. T.; Duarte, T. M.; Jingxiang, W.; Tao, W.; Sen, W.; Yan, X.; Le, Z.; Eli, Z.-C. The golden age of thermally activated delayed fluorescence materials: design and exploitation. *Chem. Rev.* **2024**, *124*, 13736−14110.
(11) Madayanad Suresh, S.; Hall, D.; Beljonne, D.; Olivier, Y.; Zysman-Colman, E. Multiresonant thermally activated delayed fluorescence emitters based on heteroatom-doped nanographenes: recent advances and prospects for organic light-emitting diodes. *Adv. Funct. Mater.* **2020**, *30*, No. 1908677.
(12) Park, J.; Lim, J.; Lee, J. H.; Jang, B.; Han, J. H.; Yoon, S. S.; Lee, J. Y. Asymmetric Blue Multiresonance TADF Emitters with a Narrow Emission Band. *ACS Appl. Mater. Interfaces* **2021**, *13*, 45798−45805.
(13) Oda, S.; Kawakami, B.; Kawasumi, R.; Okita, R.; Hatakeyama, T. Multiple resonance effect-induced sky-blue thermally activated delayed fluorescence with a narrow emission band. *Org. Lett.* **2019**, *21*, 9311−9314.
(14) Oda, S.; Sugitani, T.; Tanaka, H.; Tabata, K.; Kawasumi, R.; Hatakeyama, T. Development of Pure Green Thermally Activated Delayed Fluorescence Material by Cyano Substitution. *Adv. Mater.* **2022**, *34*, No. 2201778.
(15) Zhang, Y.; Zhang, D.; Wei, J.; Liu, Z.; Lu, Y.; Duan, L. Multi-resonance induced thermally activated delayed fluorophores for narrowband green OLEDs. *Angew. Chem., Int. Ed.* **2019**, *58*, 16912−16917.
(16) Huang, F.; Wang, K.; Shi, Y.-Z.; Fan, X.-C.; Zhang, X.; Yu, J.; Lee, C.-S.; Zhang, X.-H. Approaching Efficient and Narrow RGB Electroluminescence from D−A-Type TADF Emitters Containing an Identical Multiple Resonance Backbone as the Acceptor. *ACS Appl. Mater. Interfaces* **2021**, *13*, 36089−36097.
(17) Hall, D.; Suresh, S. M.; dos Santos, P. L.; Duda, E.; Bagnich, S.; Pershin, A.; Rajamalli, P.; Cordes, D. B.; Slawin, A. M. Z.; Beljonne, D.; Köhler, A.; Samuel, I. D. W.; Olivier, Y.; Zysman-Colman, E. Improving Processability and Efficiency of Resonant TADF Emitters: A Design Strategy. *Adv. Opt. Mater.* **2020**, *8*, No. 1901627.
(18) Yang, M.; Park, I. S.; Yasuda, T. Full-Color, Narrowband, and High-Efficiency Electroluminescence from Boron and Carbazole Embedded Polycyclic Heteroaromatics. *J. Am. Chem. Soc.* **2020**, *142*, 19468−19472.
(19) Lee, Y.-T.; Chan, C.-Y.; Tanaka, M.; Mamada, M.; Balijapalli, U.; Tsuchiya, Y.; Nakanotani, H.; Hatakeyama, T.; Adachi, C. Investigating HOMO Energy Levels of Terminal Emitters for Realizing High-Brightness and Stable TADF-Assisted Fluorescence Organic Light-Emitting Diodes. *Adv. Electron. Mater.* **2021**, *7*, No. 2001090.
(20) Qiu, X.; Tian, G.; Lin, C.; Pan, Y.; Ye, X.; Wang, B.; Ma, D.; Hu, D.; Luo, Y.; Ma, Y. Narrowband Emission from Organic Fluorescent Emitters with Dominant Low-Frequency Vibronic Coupling. *Adv. Opt. Mater.* **2021**, *9*, No. 2001845.
(21) Konidena, R. K.; Naveen, K. R. Boron-Based Narrowband Multiresonance Delayed Fluorescent Emitters for Organic Light-Emitting Diodes. *Adv. Photonics Res.* **2022**, *3*, No. 2200201.
(22) Pershin, A.; Hall, D.; Lemaur, V.; Sancho-Garcia, J.-C.; Muccioli, L.; Zysman-Colman, E.; Beljonne, D.; Olivier, Y. Highly emissive excitons with reduced exchange energy in thermally activated delayed fluorescent molecules. *Nat. Commun.* **2019**, *10*, No. 597.
(23) Han, S. H.; Jeong, J. H.; Yoo, J. W.; Lee, J. Y. Ideal blue thermally activated delayed fluorescence emission assisted by a thermally activated delayed fluorescence assistant dopant through a fast reverse intersystem crossing mediated cascade energy transfer process. *J. Mater. Chem. C* **2019**, *7*, 3082−3089.
(24) Hatakeyama, T.; Shiren, K.; Nakajima, K.; Nomura, S.; Nakatsuka, S.; Kinoshita, K.; Ni, J.; Ono, Y.; Ikuta, T. Ultrapure Blue Thermally Activated Delayed Fluorescence Molecules: Efficient HOMO-LUMO Separation by the Multiple Resonance Effect. *Adv. Mater.* **2016**, *28*, 2777−2781.
(25) Ha, J. M.; Hur, S. H.; Pathak, A.; Jeong, J.-E.; Woo, H. Y. Recent advances in organic luminescent materials with narrowband emission. *NPG Asia Mater.* **2021**, *13*, No. 53.
(26) Nikhitha, R.; Mondal, A. Breaking the trade-off between ΔE_{ST} and oscillator strength in hybrid LR/SR-CT compounds for enhanced TADF performance. *J. Mater. Chem. C* **2025**, *13*, 1893−1906.
(27) Sanyam; Khatua, R.; Mondal, A. Constructing Multiresonance Thermally Activated Delayed Fluorescence Emitters for Organic LEDs: A Computational Investigation. *J. Phys. Chem. A* **2023**, *127*, 10393−10405.
(28) Guan, J.; Shen, C.; Peng, J.; Zheng, J. What leads to aggregation-induced emission? *J. Phys. Chem. Lett.* **2021**, *12*, 4218−4226.
(29) Valverde, D.; Ser, C. T.; Ricci, G.; Jorner, K.; Pollice, R.; Aspuru-Guzik, A.; Olivier, Y. Computational Investigations of the Detailed Mechanism of Reverse Intersystem Crossing in Inverted Singlet−Triplet Gap Molecules. *ACS Appl. Mater. Interfaces.* **2024**, *16*, 66991−67001.
(30) Rukin, P. S.; Fortino, M.; Prezzi, D.; Rozzi, C. A. Complementing Adiabatic and Nonadiabatic Methods To Understand Internal Conversion Dynamics in Porphyrin Derivatives. *J. Chem. Theory Comput.* **2024**, *20*, 10759−10769.
(31) Chen, X.-K.; Kim, D.; Brédas, J.-L. Thermally activated delayed fluorescence (TADF) path toward efficient electroluminescence in purely organic materials: molecular level insight. *Acc. Chem. Res.* **2018**, *51*, 2215−2224.
(32) Qian, Y.; Li, X.; Harutyunyan, A. R.; Chen, G.; Rao, Y.; Chen, H. Herzberg−Teller effect on the vibrationally resolved absorption spectra of single-crystalline pentacene at finite temperatures. *J. Phys. Chem. A* **2020**, *124*, 9156−9165.
(33) Lv, L.; Liu, K.; Yuan, K.; Zhu, Y.; Wang, Y. Thermally activated delayed fluorescence processes for Cu (i) complexes in solid-state: a computational study using quantitative prediction. *RSC Adv.* **2018**, *8*, 28421−28432.
(34) Kundu, S.; Roy, P. P.; Fleming, G. R.; Makri, N. Franck−Condon and Herzberg−Teller signatures in molecular absorption and emission spectra. *J. Phys. Chem. B* **2022**, *126*, 2899−2911.
(35) Roy, P. P.; Kundu, S.; Makri, N.; Fleming, G. R. Interference between Franck−Condon and Herzberg−Teller terms in the condensed-phase molecular spectra of metal-based tetrapyrrole derivatives. *J. Phys. Chem. Lett.* **2022**, *13*, 7413−7419.
(36) Ghosh, P.; Alvertis, A. M.; Chowdhury, R.; Murto, P.; Gillett, A. J.; Dong, S.; Sneyd, A. J.; Cho, H.-H.; Evans, E. W.; Monserrat, B.; Feng, L.; Christoph, S.; Hugo, B.; H, F. R.; Akshay, R. Decoupling

https://doi.org/10.1021/acsaelm.5c00286
ACS Appl. Electron. Mater. XXXX, XXX, XXX−XXX

excitons from high-frequency vibrations in organic molecules. *Nature* **2024**, *629*, 355−362.
(37) Penfold, T. J.; Gindensperger, E.; Daniel, C.; Marian, C. M. Spin-vibronic mechanism for intersystem crossing. *Chem. Rev.* **2018**, *118*, 6975−7025.
(38) Wei, X.; Li, Z.; Hu, T.; Duan, R.; Liu, J.; Wang, R.; Liu, Y.; Hu, X.; Yi, Y.; Wang, P.; Wang, Y. Substitution conformation balances the oscillator strength and singlet−triplet energy gap for highly efficient D−A−D thermally activated delayed fluorescence emitters. *Adv. Opt. Mater.* **2019**, *7*, No. 1801767.
(39) Wang, Z.; Li, Y.; Cai, X.; Chen, D.; Xie, G.; Liu, K.; Wu, Y.-C.; Lo, C.-C.; Lien, A.; Cao, Y.; Su, S. J. Structure−performance investigation of thioxanthone derivatives for developing color tunable highly efficient thermally activated delayed fluorescence emitters. *ACS Appl. Mater. Interfaces* **2016**, *8*, 8627−8636.
(40) Wang, H.; Xie, L.; Peng, Q.; Meng, L.; Wang, Y.; Yi, Y.; Wang, P. Novel thermally activated delayed fluorescence materials−thioxanthone derivatives and their applications for highly efficient OLEDs. *Adv. Mater.* **2014**, *26*, 5198−5204.
(41) Wei, X.; Chen, Y.; Duan, R.; Liu, J.; Wang, R.; Liu, Y.; Li, Z.; Yi, Y.; Yamada-Takamura, Y.; Wang, P.; Wang, Y. Triplet decay-induced negative temperature dependence of the transient photoluminescence decay of thermally activated delayed fluorescence emitter. *J. Mater. Chem. C* **2017**, *5*, 12077−12084.
(42) Wex, B.; Kaafarani, B. R. Perspective on carbazole-based organic compounds as emitters and hosts in TADF applications. *J. Mater. Chem. C* **2017**, *5*, 8622−8653.
(43) Frisch, M. J.; Trucks, G. W.; Schlegel, H. B.; Scuseria, G. E.; Robb, M. A.; Cheeseman, J. R.; Scalmani, G.; Barone, V.; Mennucci, B.; Petersson, G. A.; Nakatsuji, H.; Caricato, M.; Li, X.; Hratchian, H. P.; Izmaylov, A. F.; Bloino, J.; Zheng, G.; Sonnenberg, J. L.; Hada, M.; Ehara, M.; Toyota, K.; Fukuda, R.; Hasegawa, J.; Ishida, M.; Nakajima, T.; Honda, Y.; Kitao, O.; Nakai, H.; Vreven, T.; Montgomery, J. A., Jr.; Peralta, J. E.; Ogliaro, F.; Bearpark, M.; Heyd, J. J.; Brothers, E.; Kudin, K. N.; Staroverov, V. N.; Kobayashi, R.; Normand, J.; Raghavachari, K.; Rendell, A.; Burant, J. C.; Iyengar, S. S.; Tomasi, J.; Cossi, M.; Rega, N.; Millam, J. M.; Klene, M.; Knox, J. E.; Cross, J. B.; Bakken, V.; Adamo, C.; Jaramillo, J.; Gomperts, R.; Stratmann, R. E.; Yazyev, O.; Austin, A. J.; Cammi, R.; Pomelli, C.; Ochterski, J. W.; Martin, R. L.; Morokuma, K.; Zakrzewski, V. G.; Voth, G. A.; Salvador, P.; Dannenberg, J. J.; Dapprich, S.; Daniels, A. D.; Farkas; Foresman, J. B.; Ortiz, J. V.; Cioslowski, J.; Fox, D. J. *Gaussian 09*, Revision E.01; Gaussian Inc: Wallingford CT, 2009.
(44) Adamo, C.; Barone, V. Toward reliable density functional methods without adjustable parameters: The PBE0 model. *J. Chem. Phys.* **1999**, *110*, 6158−6170.
(45) Loos, P.-F.; Jacquemin, D. Evaluating 0−0 energies with theoretical tools: A short review. *ChemPhotoChem* **2019**, *3*, 684−696.
(46) Neese, F. The ORCA program system. *WIREs Comput. Mol. Sci.* **2012**, *2*, 73−78.
(47) Xu, S.; Yang, Q.; Wan, Y.; Chen, R.; Wang, S.; Si, Y.; Yang, B.; Liu, D.; Zheng, C.; Huang, W. Predicting intersystem crossing efficiencies of organic molecules for efficient thermally activated delayed fluorescence. *J. Mater. Chem. C* **2019**, *7*, 9523−9530.
(48) Aizawa, N.; Harabuchi, Y.; Maeda, S.; Pu, Y.-J. Kinetic prediction of reverse intersystem crossing in organic donor−acceptor molecules. *Nat. Commun.* **2020**, *11*, No. 3909.
(49) Sánchez-Carrera, R. S.; Paramonov, P.; Day, G. M.; Coropceanu, V.; Brédas, J.-L. Interaction of charge carriers with lattice vibrations in oligoacene crystals from naphthalene to pentacene. *J. Am. Chem. Soc.* **2010**, *132*, 14437−14446.
(50) Del Valle, J. C.; Catalán, J. Kasha's rule: a reappraisal. *Phys. Chem. Chem. Phys.* **2019**, *21*, 10061−10069.
(51) Lower, S. K.; El-Sayed, M. The triplet state and molecular electronic processes in organic molecules. *Chem. Rev.* **1966**, *66*, 199−241.
(52) Souza, J.; Benatto, L.; Candiotto, G.; Wouk, L.; Koehler, M. Dynamics of vibrationally coupled intersystem crossing in state-of-the-art organic optoelectronic materials. *Commun. Chem.* **2025**, *8*, No. 84.
(53) Gruhn, N. E.; da Silva Filho, D. A.; Bill, T. G.; Malagoli, M.; Coropceanu, V.; Kahn, A.; Brédas, J.-L. The vibrational reorganization energy in pentacene: molecular influences on charge transport. *J. Am. Chem. Soc.* **2002**, *124*, 7918−7919.

https://doi.org/10.1021/acsaelm.5c00286
ACS Appl. Electron. Mater. XXXX, XXX, XXX−XXX